nature communications

Article

https://doi.org/10.1038/s41467-022-35372-5

Quantification of gas-accessible micro-porosity in metal-organic framework glasses

Received: 20 December 2021

Accepted: 30 November 2022

Published online: 14 December 2022

Check for updates

Louis Frentzel-Beyme [1], Pascal Kolodzeiski[1], Jan-Benedikt Weiß [1], Andreas Schneemann [2] & Sebastian Henke [1]

Metal-organic framework (MOF) glasses are a new class of glass materials with immense potential for applications ranging from gas separation to optics and solid electrolytes. Due to the inherent difficulty to determine the atomistic structure of amorphous glasses, the intrinsic structural porosity of MOF glasses is only poorly understood. Here, we investigate the porosity features (pore size and pore limiting diameter) of a series of prototypical MOF glass formers from the family of zeolitic imidazolate frameworks (ZIFs) and their corresponding glasses. CO_2 sorption at 195 K allows quantifying the micro-porosity of these materials in their crystalline and glassy states, also providing excess to the micropore volume and the apparent density of the ZIF glasses. Additional hydrocarbon sorption data together with X-ray total scattering experiments prove that the porosity features of the ZIF glasses depend on the types of organic linkers. This allows formulating design principles for a targeted tuning of the intrinsic microporosity of MOF glasses. These principles are counterintuitive and contrary to those established for crystalline MOFs but show similarities to strategies previously developed for porous polymers.

Metal-organic frameworks (MOFs) are permanently porous crystalline materials with well-defined ordered structures, which can be precisely designed by a number of advanced synthetic concepts[1–4]. In the past two decades, MOFs have grown to a class of modular materials with widely tuneable properties for applications ranging from gas separation and storage to sensing, drug delivery and catalysis[5–9]. MOFs have also been proposed for applications in fields less common for porous materials, such as solid electrolytes and (opto)electronics[10,11]. In recent years defective, disordered and amorphous MOFs have gained more and more attention since these materials provide access to new and unusual properties beyond the state of the art[12–20]. Especially solid-to-liquid transitions of MOFs are exciting, as they offer processing and shaping of the framework materials in their liquid state (i.e. above their melting temperature, T_m) and vitrification to a MOF glass after cooling below their glass transition temperature (T_g)[21–25]. MOF glasses propose unique opportunities for solid-state ion conduction[20,26,27] and gas separation membranes[28–30] because of improved performance as a result of their monolithic structure and the absence of mass transport limiting grain boundaries[31]. However, compared to their structurally well-defined crystalline parent materials, it is very difficult to predict and design the functionally relevant porosity features (pore volume and pore size) of the MOF glasses. This is due to their highly disordered structure lacking any long-range order, thus precluding atomistic structure determination[32]. Knowledge of the atomistic structure of porous framework materials, however, is the foundation of materials design along the principles of reticular chemistry[33].

Zeolitic imidazolate frameworks (ZIFs) are the best-investigated family of meltable and glass-forming MOFs. ZIFs are composed of tetrahedrally coordinated metal ions (typically Zn^{2+} or Co^{2+}), which are interconnected by imidazolate linkers to form crystalline frameworks exhibiting strong structural similarities to inorganic zeolites[34,35]. Even though more than 250 crystalline ZIFs featuring >50 different network topologies have been reported thus far[36], just very few of these have been demonstrated to melt and form glasses via melt-quenching. The reported ZIF glass formers include frameworks with **cag** (ZIF-4, ZIF-62, TIF-4, ZIF-UC-1 to ZIF-UC-5), **zni** (ZIF-zni) and **gis** (denoted $Zn(im)_2$

[1]Anorganische Chemie, Fakultät für Chemie & Chemische Biologie, Technische Universität Dortmund, Otto-Hahn Straße 6, 44227 Dortmund, Germany. [2]Anorganische Chemie I, Technische Universität Dresden, Bergstrasse 66, 01069 Dresden, Germany. e-mail: sebastian.henke@tu-dortmund.de

(GIS)) topologies[23,37–39] (a graphical representation of the network topologies is given in Supplementary Fig. 1). Meltable ZIFs of these topologies have further been shown to act as a flux for the melting of other ZIF structure types that are non-meltable on their own (i.e. ZIF-76, **lta** topology; ZIF-8, **sod** topology)[40–42]. Given that the crystalline ZIF precursors are typically microporous solids with porosity features interesting for gas storage and separation[43–47], their melt-quenched glasses are deemed to exhibit similar potential for gas adsorption and separation processes[28,29]. Nevertheless, gas-accessible microporosity in MOF glasses has only been poorly investigated and was just demonstrated for a few ZIF glasses[30,37,38,48]. Quantification of the total gas-accessible pore volume of the ZIF glasses as well as a comprehensive comparison of the porosity of the glasses in relation to their crystalline precursors has not yet been reported. Understanding the porosity features of ZIF glasses, however, is of utmost importance for their application in many fields, e.g. gas separation membranes[28] and solid electrolytes[20].

The prototypical MOF glass former is ZIF-4. During thermal treatment crystalline ZIF-4 first collapses to the amorphous phase a_TZIF-4 (a_T denotes thermally amorphized) at around 315 °C, followed by recrystallization to a denser polymorph of **zni** topology at ~460 °C (this phase is denoted by zni_TZIF-4 here, i.e. thermally recrystallized ZIF-4 with **zni** topology) and finally melting at about 580 °C (Fig. 1)[21]. Quenching the ZIF-4 melt to room temperature generates a glass named a_gZIF-4 (a_g denotes amorphous glass)[23,49]. Positron annihilation lifetime spectroscopy (PALS) revealed that a_gZIF-4 possesses residual microporosity[50]; a finding supported by high-level molecular dynamics simulations[51,52]. Thereon, PALS has been employed to investigate the porosity of other MOF glasses[28,40,42,53]. The method, however, is unable to prove that the detected pores in the ZIF glasses are in fact accessible to gas molecules, i.e. that the glasses possess an open framework[50]. Moreover, it is very difficult to quantify porosity (i.e. to determine the specific pore volume of the solid) with PALS[54].

Isothermal N_2 physisorption at 77 K or Ar physisorption at 87 K is widely applied for the quantification of porosity and surface area of crystalline as well as amorphous porous materials[55,56]. For a variety of technologically relevant amorphous porous materials (e.g. amorphous silica and amorphous carbons) cryogenic N_2 and Ar sorption were successfully applied to get valuable insights into the porosity and thus the structure of these materials[56]. While Ar sorption of ZIF glasses has not been studied yet, previous work demonstrated that N_2 is not adsorbed at 77 K in any ZIF glass investigated so far (i.e. a_gZIF-4, a_gZIF-62 and a_gZIF-UC-2 to a_gZIF-UC-5)[21,30,38]; a phenomenon ascribed to diffusion limitations of N_2 gas into the narrow pores of the ZIF glasses at this low temperature[38,57]. Microporosity for some mixed-linker ZIF glasses was nevertheless demonstrated with CO_2 physisorption measurements at 273 or 298 K with a maximum CO_2 pressure of about 95 kPa (Supplementary Table 6). Even though such measurements provide experimental proof for gas-accessible microporosity in these ZIF glasses, they do not allow quantification of the major parameter of porosity, namely the pore volume. This is because the sorption data are collected too far away from saturation (note, a CO_2 gas pressure of 100 kPa corresponds to a relative pressure (p/p_0) of only about 0.03 at 273 K[57])[58].

In this work, we demonstrate that CO_2 gas sorption measurements at 195 K together with various hydrocarbon sorption measurements provide deep insights into the intrinsic porosity (particularly the pore volume) of ZIF glasses. Under the established assumption that CO_2 is present in its supercooled liquid state when confined in micropores at 195 K[59,60], a p/p_0 of 0.52 is reached at an absolute pressure of 100 kPa. At such a relative pressure the micropores of the porous ZIF glasses are completely filled with adsorbate, so that their specific micropore volume can be quantified from the amount adsorbed. This allows us to set the porosity of the ZIF glasses in relation to the porosity of their crystalline ZIF precursors. In addition to the canonical glass formers ZIF-4 and ZIF-zni (composition $Zn(im)_2$ for both; im^- = imidazolate), the mixed-linker glass-forming frameworks ZIF-62 (composition $Zn(im)_{1.65}(bim)_{0.35}$; bim^- = benzimidazolate) and TIF-4 (composition $Zn(im)_{1.68}(mbim)_{0.32}$; $mbim^-$ = 5-methylbenzimidazolate) are also studied (Fig. 1). While ZIF-4 is particularly interesting due to the series of reconstructive crystalline-to-amorphous-to-crystalline phase transitions (ZIF-4 to a_TZIF-4 to zni_TZIF-4) before melting

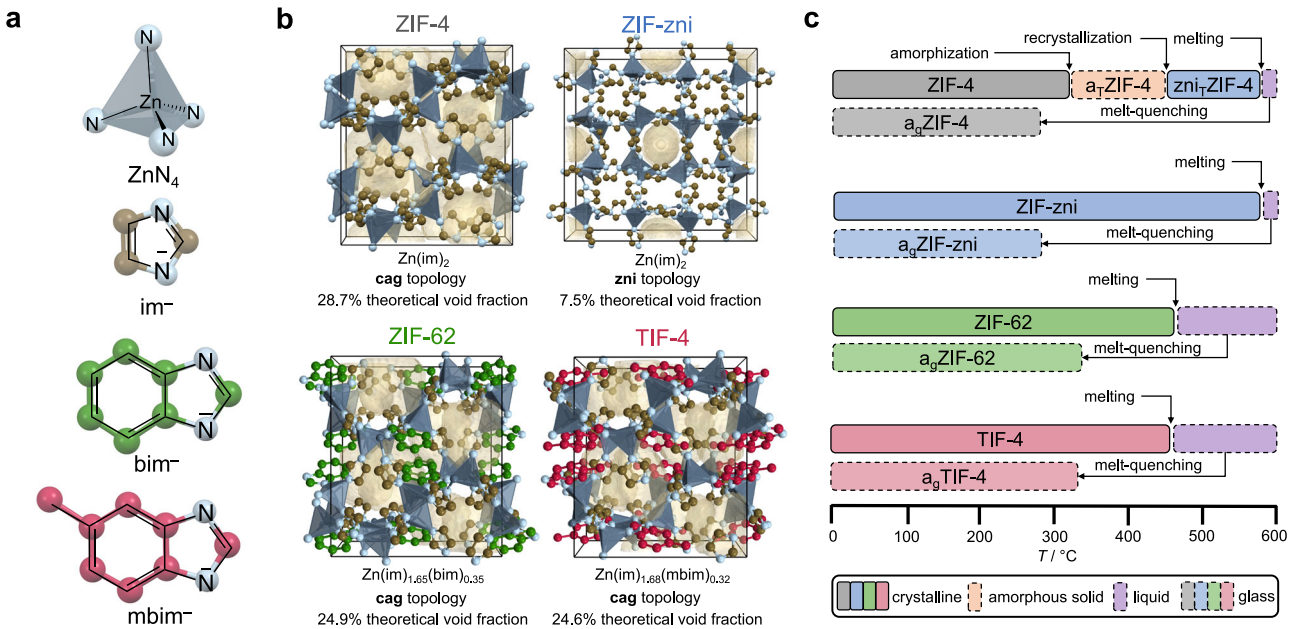

Fig. 1 | Structural representations and high-temperature phase behaviour of the investigated ZIF glass formers. a Building units of the investigated ZIF glass formers. **b** Crystal structures of the ZIF glass formers. ZIF-4 (CCDC code IMIDZB11), ZIF-62 (CCDC code SIWJAM) and TIF-4 (CCDC code QOSYAZ) are viewed along the crystallographic *b*-axis. ZIF-zni (CCDC code IMIDZB) is viewed along the crystallographic *c*-axis. Hydrogen atoms are omitted for clarity. The theoretical void fraction was calculated with a probe radius of 1.6 Å (see Supplementary Methods 9.4 for further details) and is shown in pale yellow. **c** Schematic representation of the high-temperature phase behaviour of the ZIF glass formers.

at ~580 °C (Fig. 1c), ZIF-62 and TIF-4 are relevant because of their lower melting temperatures and more complex structure incorporating a secondary bulky imidazolate linker besides the simple im^- linker. The derived specific pore volumes of the ZIF glasses are directly connected to the material's apparent density (ρ_{app}), i.e. the density including the intrinsic microporosity, $\rho_{app} = m/(V_{frame} + V_{pore})$; with m = mass, V_{frame} = volume of the framework, V_{pore} = pore volume)[61]. ρ_{app} is an important physical parameter, so far poorly investigated for ZIF glasses. Previous studies utilizing He pycnometry[23,38,42] could only determine the skeletal density (ρ_{skl}) of the glasses (that is the density excluding the intrinsic microporosity, $\rho_{skl} = m/V_{frame}$). Similarly, density measurements based on Archimedes' principle with potentially pore-filling fluids (i.e. ethanol) are also expected to yield skeletal densities[62,63]. Combining the low-temperature CO_2 sorption data with additional hydrocarbon sorption experiments and structural insights derived from X-ray total scattering experiments allows deducing important correlations of the chemical composition of the ZIF glass former (i.e. single linker or mixed-linker materials) with the pore volume and the pore size of the derived MOF glass. Unexpectedly and most importantly, the relationship between the steric bulk of the linkers and the porosity features of the glasses is counterintuitive and found to be inverse to what is established for crystalline MOFs. The work provides a guideline for the targeted design of MOF glass porosity by a selection of the frameworks' building blocks.

Results

Materials preparation and characterization

ZIF-4 ($Zn(im)_2$, **cag** topology), ZIF-zni ($Zn(im)_2$, **zni** topology), ZIF-62 ($Zn(im)_{1.65}(bim)_{0.35}$, **cag** topology) and TIF-4 ($Zn(im)_{1.68}(mbim)_{0.32}$, **cag** topology) were synthesized solvothermally reproducing or adapting established procedures[30]. Solvent molecules were removed from the materials at 200 °C under a dynamic vacuum yielding the activated (solvent-free) compounds. The phase purity of the crystalline ZIFs was verified by structureless profile fits (Pawley method[64]) of X-ray powder diffraction (XRPD) patterns using reference data from the literature (Supplementary Figs. 2–6)[45,65–67]. The complete removal of solvents from the pores is demonstrated by ^{1}H nuclear magnetic resonance (NMR) and Fourier-transform infra-red (FTIR) spectroscopy data (see Supplementary Methods 3, 4 for further details). ^{1}H NMR spectroscopy was further used to determine the linker ratio of the ZIF-62 and TIF-4 samples, leading to the chemical compositions given above (Supplementary Figs. 21, 23).

Based on the four crystalline reference materials, the corresponding thermal products (a_TZIF-4, zni_TZIF-4, a_gZIF-4, a_gZIF-zni, a_gZIF-62 and a_gTIF-4, Fig. 1c) were obtained via thermal treatment under inert atmosphere in a thermogravimetric analysis/differential scanning calorimetry (TGA/DSC) apparatus. DSC data served as a guide for selecting the right temperature protocol to obtain the glasses, as well as the intermediate compounds a_TZIF-4 and zni_TZIF-4 in the case of ZIF-4 (Fig. 2a, Supplementary Table 2). Heating and cooling rates have been +10 and −10 °C min^{-1}, respectively. The temperature profiles and corresponding TGA/DSC data yielding the corresponding products are summarized in the Supplementary Information (Supplementary Table 4, Supplementary Figs. 27–32). We note, that for the preparation of a_gZIF-4 and a_gZIF-zni an isothermal segment (10 min) at a maximum temperature of 578 °C was required to obtain amorphous glasses without crystalline residues of ZIF-zni (Supplementary Fig. 12).

All products were characterized with XRPD and X-ray total scattering, ^{1}H NMR and FTIR spectroscopy, as well as DSC, and the obtained data are in agreement with the literature[21,23,30,39,53,67,68]. XRPD data of the amorphous materials show only diffuse scattering and no sharp Bragg peaks (Fig. 2b, Supplementary Figs. 7–11). A profile fit to the XRPD pattern of zni_TZIF-4 testifies the recrystallization of a_TZIF-4 to the $Zn(im)_2$ phase with **zni** topology (Supplementary Fig. 4). The glasses a_gZIF-4, a_gZIF-zni, a_gZIF-62 and a_gTIF-4 further display particle coalescence characteristic for melt-quenched glasses (Supplementary Figs. 33–36). It is noteworthy that ^{1}H NMR data of digested ZIF samples demonstrate the full integrity of the organic linkers after thermal treatment, except for a_gZIF-4 and a_gZIF-zni (Fig. 2c, Supplementary Figs. 16–18, 20, 22, 24). For the latter glasses, weak signals for impurities are visible in their ^{1}H NMR spectra. These impurities are ascribed to the presence of some decomposition products which are a consequence of the higher maximum processing temperature (578 °C) of these two glass materials compared to a_gZIF-62 and a_gTIF-4 (maximum processing temperature is 475 °C for those glasses). Partial decomposition of a_gZIF-4 and a_gZIF-zni is further indicated by weak scattering signals ascribed to crystalline ZnO impurities in their X-ray total scattering functions $S(Q)$ (Fig. 2d, Suppplementary Figs. 41, 43), mass losses of about 6% during glass preparation in the TGA/DSC experiment (Supplementary Figs. 29, 30), as well as the dark colour of these glasses (Supplementary Figs. 33, 34). The other three amorphous materials (a_TZIF-4, a_gZIF-62 and a_gTIF-4) show neither signs of decomposition of the organic linkers nor the formation of crystalline by-products.

X-ray pair distribution functions (XPDFs) in the form of $D(r)$ derived via Fourier-transformation of the total scattering functions $S(Q)$[69] of all crystalline ZIFs and their thermal products demonstrate that the short-range structure of the crystalline phases (that is Zn^{2+} ions surrounded by four imidazolate-type linkers) is preserved in all amorphous phases (Fig. 2d, e, see Supplementary Methods 8 and Supplementary Figs. 41, 42). The last sharp peak in the XPDFs of the amorphous materials is visible at about 5.9 Å and corresponds to the distance of two neighbouring Zn^{2+} ions in the networks. The XPDFs of a_TZIF-4, a_gZIF-62 and a_gTIF-4 show some weaker correlations for $r > 5.9$ Å, which are indicative of some medium-range order (MRO). At $r > 15$ Å, $D(r)$ of these materials converges towards zero. In contrast, the XPDFs of a_gZIF-4 and a_gZIF-zni show additional weak but significant pair correlations extending well beyond $r = 20$ Å (Supplementary Fig. 42). These correlations are ascribed to the crystalline ZnO impurities present in these ZIF glasses (Supplementary Fig. 43).

With the aim to get more insights into the structure of the amorphous ZIF derivatives, we take a closer look at the first sharp diffraction peak (FSDP) of their scattering functions $S(Q)$ (Fig. 2d). The FSDP contains valuable information about the MRO of amorphous network solids[70–72]. For the ZIF glasses, MRO means some degrees of order extending beyond the first Zn–Zn neighbour distance. The position of the FSDP (Q_{FSDP}) has been associated with a real space correlation length between the strongest scattering centres (i.e. Zn^{2+} cations here), which are surrounded by interstitial voids[73,74]. As such, Q_{FSDP} could be regarded as a reciprocal space signature for the glass networks' porosity and density. The full width at half maximum of the FSDP (ΔQ_{FSDP}) is inversely proportional to the real space coherence length over which the MRO (i.e. the correlation) exists[73,74]. We fitted the FSDP of the five amorphous materials under study here to a pseudo-Voigt function to derive Q_{FSDP} and ΔQ_{FSDP} (see Supplementary Methods 8.1). Q_{FSDP} is identical for all solids found at about 1.11 Å^{-1}, suggesting the densities of a_TZIF-4 and the four glasses are similar. Remarkably, ΔQ_{FSDP} is significantly larger for a_gZIF-62 and a_gTIF-4 ($\Delta Q_{FSDP} = 0.35$ Å^{-1}) than for the amorphous ZIF-4/ZIF-zni derivatives ($\Delta Q_{FSDP} = 0.24$–0.29 Å^{-1}). This translates to a shorter coherence length for the MRO in the mixed-linker ZIF glasses. Hence, a_gZIF-62 and a_gTIF-4 are more disordered than the single-linker materials, which can be explained by their more complex chemical composition involving two different imidazolate-type linkers with different steric bulk.

N_2 and Ar physisorption studies

N_2 sorption isotherms at 77 K were collected for all crystalline and amorphous materials (Supplementary Figs. 45, 46). Only crystalline ZIF-4 (the most porous ZIF under study here) adsorbs large amounts of N_2, while all other compounds (including crystalline ZIF-62 and TIF-4) show negligible adsorption of N_2 at 77 K, preventing the determination

https://doi.org/10.1038/s41467-022-35372-5

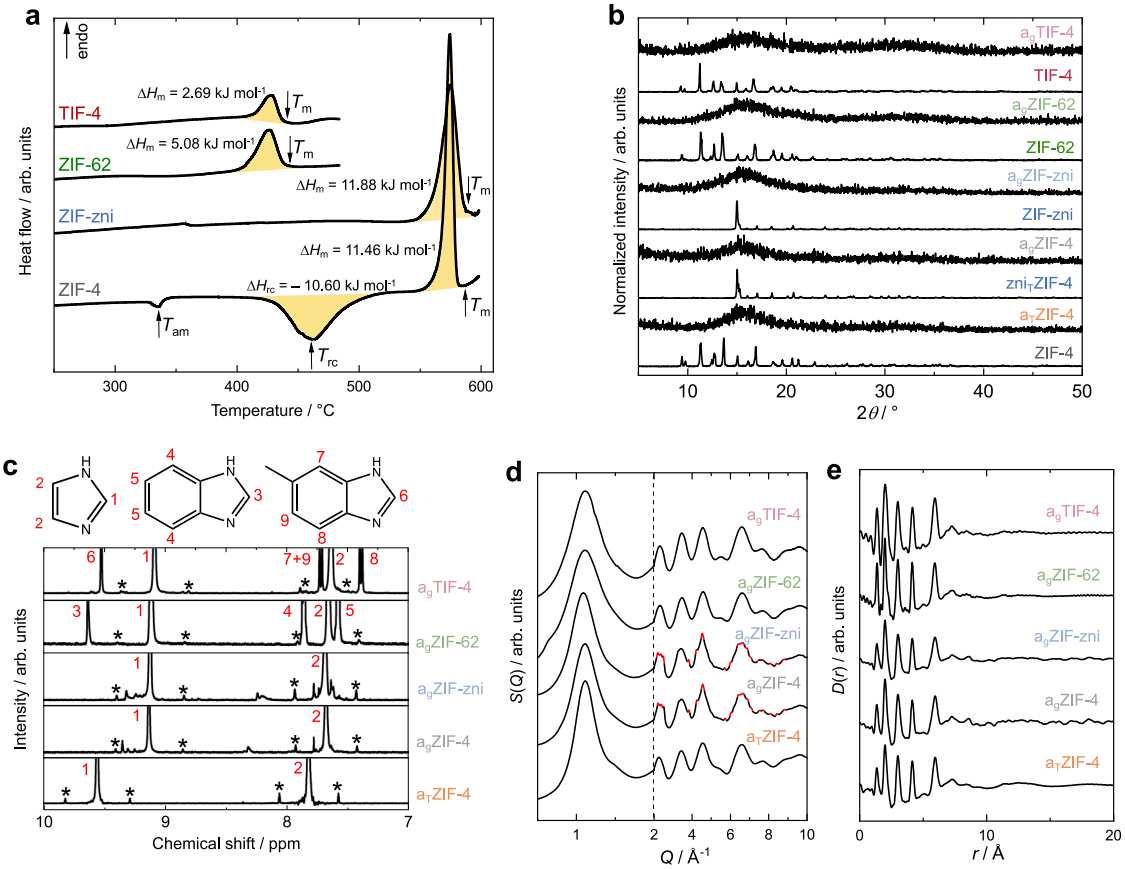

Fig. 2 | Thermal and structural characterization of the ZIF glass formers and their corresponding glasses. a DSC data of the ZIF glass formers. **b** XRPD patterns of all investigated materials. The patterns are vertically offset for clarity. **c** Stacked plot of ^{1}H NMR spectra of digested samples of the investigated amorphous materials (recorded in a solvent mixture of DMSO-d_6 and DCl/D_2O at room temperature). A zoom in the aromatic region is shown. The ^{13}C satellite peaks of protons 1 and 2 are marked with asterisks (*). Weak signals not marked with asterisks belong to unidentified decomposition products. **d** X-ray total scattering data in the form $S(Q)$ of the amorphous phases. For a_gZIF-4 and a_gZIF-zni sharp scattering features ascribed to ZnO impurities are highlighted in red. **e** XPDFs in form $D(r)$ obtained from the $S(Q)$ data shown in **d**. Data for a_gZIF-62 in panels **d** and **e** are taken from ref. 30.

of the material's pore volume. These observations are in accordance with available N_2 sorption data of ZIF glasses and point towards strong N_2 diffusion limitations at 77 K due to the narrow micropores of these ZIFs[14,21,30]. Additional N_2 sorption isotherms recorded at 195 K suggest that N_2 is able to access some of the narrow micropores of the ZIF glasses, however, the recorded uptakes are again rather low (0.25–0.45 mmol g^{-1} at 95 kPa) and large hystereses are apparent on the desorption branch, indicating that the diffusion of N_2 in and out of the pores of the ZIF glasses is still hindered at this temperature (Supplementary Fig. 47). Similarly, Ar sorption isotherms recorded at 87 K covering a p/p_0 range from 0 to 1, prove that the narrow micropores of the ZIF glasses are largely inaccessible to Ar at this temperature (Supplementary Fig. 48).

Table 1 | Summary of maximum gas capacities (n_{ads}^{max}), specific micropore volumes (V_{pore}) and BET areas (S_{BET}) obtained from the CO_2 gas physisorption isotherms collected at 195 K together with the calculated densities (ρ) for all investigated materials

Compound	n_{ads}^{max} [mmol g^{-1}]	V_{pore} [cm^3 g^{-1}]	S_{BET} [m^2 g^{-1}]	ρ [g cm^{-3}]
ZIF-4	7.22	0.25	490	1.22[a]
a_TZIF-4	2.49	0.09	145	1.39[b]
zni_TZIF-4	1.23	0.04	92	1.54[a]
a_gZIF-4	2.84	0.10	187	1.38[b]
ZIF-zni	1.21	0.04	94	1.54[a]
a_gZIF-zni	3.12	0.11	189	1.36[b]
ZIF-62	4.70	0.16	264	1.29[a]
a_gZIF-62	3.34	0.12	200	1.35[b]
TIF-4	3.76	0.13	185	1.32[a]
a_gTIF-4	3.40	0.12	204	1.35[b]

[a]Crystallographic density.
[b]Apparent density (ρ_{app}) calculated from CO_2 sorption data.

CO_2 physisorption studies and pore volume determination

In order to get around the gas diffusion limitations, the porosity of all materials was probed by CO_2 physisorption at 195 K. The smaller kinetic diameter of the CO_2 molecule (3.30 Å[75]) compared to N_2 (3.64 Å[75]) and Ar (3.40 Å[75]) together with the higher temperature (195 vs. 77 K) facilitates the diffusion of the gas into narrow micropores (size < 5 Å)[76,77]. Compared to the CO_2 sorption experiments performed at 273 or 298 K, running the experiment at 195 K allows complete filling of the micropores at 100 kPa[78]. In a non- or macroporous system, CO_2 solidifies at the given conditions. In microporous materials (i.e. pores with a size ≤ 20 Å), CO_2 is considered to be in its supercooled liquid state so that the micropores are effectively filled with fluid CO_2 and not with solid CO_2[59,60]. The saturation pressure (p_0) for the gas/supercooled-liquid equilibrium is significantly higher (p_0 = 191 kPa at 195 K) than p_0 for the gas/solid equilibrium (p_0 = 100 kPa at 195 K)[79]. Hence, the maximum p/p_0 achievable in a CO_2 sorption experiment of

https://doi.org/10.1038/s41467-022-35372-5

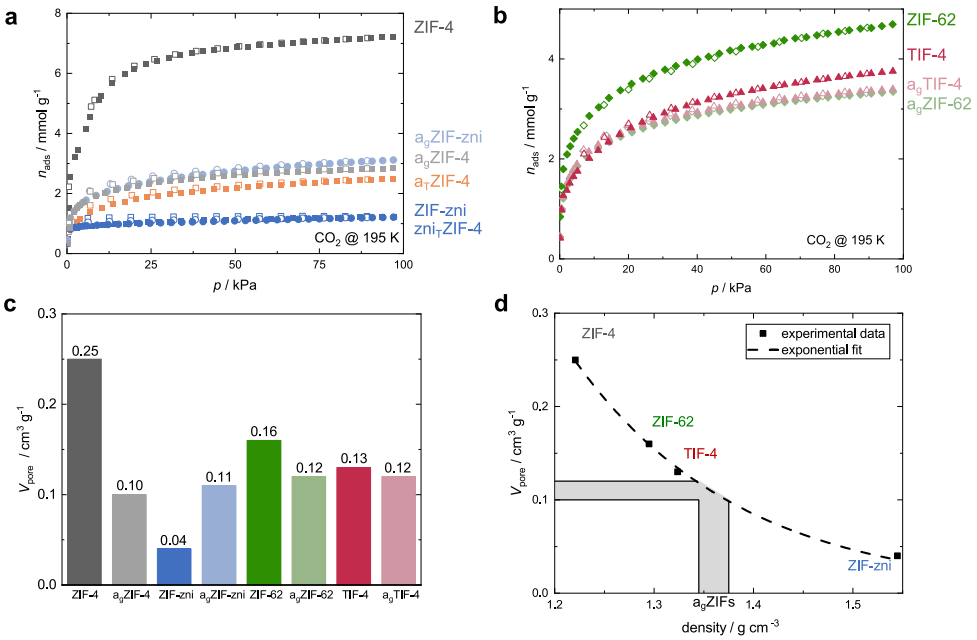

Fig. 3 | CO_2 gas sorption analysis. a CO_2 sorption isotherms collected at 195 K of ZIF-4 and ZIF-zni and their corresponding thermal products. ZIF-4 derivatives are shown as squares. ZIF-zni derivatives are shown as circles. **b** CO_2 isotherms collected at 195 K of ZIF-62 and TIF-4 and their corresponding glasses. ZIF-62 derivatives are shown as rhombs. TIF-4 derivatives are shown as triangles. In panels **a** and **b** adsorption and desorption, branches are shown as closed and open symbols, respectively. **c** Bar plot of the micropore volumes (V_{pore}) for all crystalline ZIFs and their corresponding glasses derived from the CO_2 isotherms at 195 K. **d** Plot of density against V_{pore} of all crystalline ZIFs with the exponential fit. The ZIF glass bulk densities can be estimated based on their experimentally obtained V_{pore} (see light grey area).

microporous materials at 195 K is ~0.5. Nevertheless, at this relative pressure, all pores up to a width of 50 Å are completely filled[77,78]. Consequently, the maximum gas capacities (n_{ads}^{max}) determined at 95 kPa ($p/p_0 \approx 0.5$) can be used to determine the specific micropore volume (V_{pore}) of the investigated materials by taking into account the density of supercooled liquid CO_2 at 195 K (Table 1, Fig. 3, see Supplementary Methods 9.2 for further details).

Brunauer–Emmett–Teller (BET) specific surface areas[80] have also been determined from the low-temperature CO_2 sorption isotherms (Table 1, see Supplementary Methods 9.2 for further details). Even though utilization of the BET model is very common in research on porous materials, we note that BET areas determined from CO_2 sorption data recorded at 195 K are typically much lower than values determined via N_2 sorption at 77 K[58]. In general, the BET model is not applicable to the microporous materials studied here[57]. For CO_2 sorption data recorded at 195 K, the application of the BET model is even more problematic due to the uncertainty of the effective cross-sectional area of the CO_2 molecule. Thus, we provide the BET areas of the ZIF materials only for reference.

We first concentrate on ZIF-4, ZIF-zni and their corresponding amorphous and crystalline high-temperature phases. Remarkably, all these phases adsorb CO_2 as evident from the Typ I (or Langmuir) shaped isotherms (Fig. 3a). As expected, the crystalline ZIF-4 exhibits the highest V_{pore} of 0.25 cm^3 g^{-1} (Table 1). Going along the other ZIF-4 phases consecutively formed via thermal treatment, we first see a drastic decrease in V_{pore} to 0.09 cm^3 g^{-1} for a_TZIF-4 (−64% compared to ZIF-4), demonstrating a collapse and densification of the framework but the preservation of about 36% of the pore space of the crystalline phase. V_{pore} drops further for the recrystallized zni$_T$ZIF-4 (V_{pore} = 0.04 cm^3 g^{-1}) to only about 16% of the porosity of crystalline ZIF-4. Noteworthy, the solvothermally synthesized ZIF-zni features the same pore volume (V_{pore} = 0.04 cm^3 g^{-1}) as zni$_T$ZIF-4, establishing that a_TZIF-4 completely recrystallizes to zni$_T$ZIF-4 during thermal treatment. This is in line with the very similar melting enthalpies (ΔH_{melt}) of zni$_T$ZIF-4 (11.46 kJ mol^{-1}) and ZIF-zni (11.88 kJ mol^{-1}) determined via DSC (Fig. 2a and Supplementary Table 3). Since ZIF-zni, which is the densest and most stable crystalline Zn(im)$_2$ phase (at least at temperatures >360 °C[81]), is already microporous, it is not surprising that a_gZIF-4 and a_gZIF-zni also adsorb CO_2. Both glasses show very similar CO_2 sorption isotherms with specific pore volumes of 0.10 and 0.11 cm^3 g^{-1}, respectively.

The micropore volume of the isoreticular crystalline glass precursors ZIF-4, ZIF-62 and TIF-4 decrease from 0.25 cm^3 g^{-1} (ZIF-4) to 0.16 cm^3 g^{-1} (ZIF-62) to 0.13 cm^3 g^{-1} (TIF-4). This correlates with the implementation of the secondary bulky imidazolate linkers (bim$^-$ and mbim$^-$) in ZIF-62 and TIF-4, reducing the void space of the crystalline framework (see void fractions calculated based on the crystal structures shown in Fig. 1b). We note that the concentration of the bim$^-$ and mbim$^-$ linkers in the mixed linker MOFs is rather similar (ZIF-62: Zn(im)$_{1.65}$(bim)$_{0.35}$; TIF-4: Zn(im)$_{1.68}$(mbim)$_{0.32}$), while the steric bulk of mbim$^-$ (containing an additional methyl group) is higher compared to bim$^-$. This further decreases the free void space in crystalline TIF-4 and explains the higher V_{pore} of ZIF-62 over TIF-4 (Fig. 3c).

Remarkably, the pore volumes of the mixed-linker glasses a_gZIF-62 (V_{pore} = 0.12 cm^3 g^{-1}) and a_gTIF-4 (V_{pore} = 0.12 cm^3 g^{-1}) are slightly higher than for a_gZIF-4 and a_gZIF-zni. This is counterintuitive by comparing the pore volumes of the respective crystalline parent materials. The highest reduction in V_{pore} (~60%) from the crystalline to the glass material is found for ZIF-4, while only a reduction of 25% and 8% is found for the glasses of ZIF-62 and TIF-4. This observation suggests that a_gZIF-62 and a_gTIF-4 have a pore structure that is more similar to that of their crystalline precursors, while a_gZIF-4 differs strongly from crystalline ZIF-4.

It must be noted that the presence of small amounts of decomposition products (ZnO and decomposed organic linkers) in a_gZIF-4 and a_gZIF-zni could potentially reduce the specific gas capacities and the corresponding V_{pore}. Nevertheless, the thermally amorphized phase a_TZIF-4, which does not contain any decomposition products, features an even lower pore volume (V_{pore} = 0.09 cm^3 g^{-1}) than a_gZIF-4 and a_gZIF-zni, suggesting that their partial decomposition only has a

https://doi.org/10.1038/s41467-022-35372-5

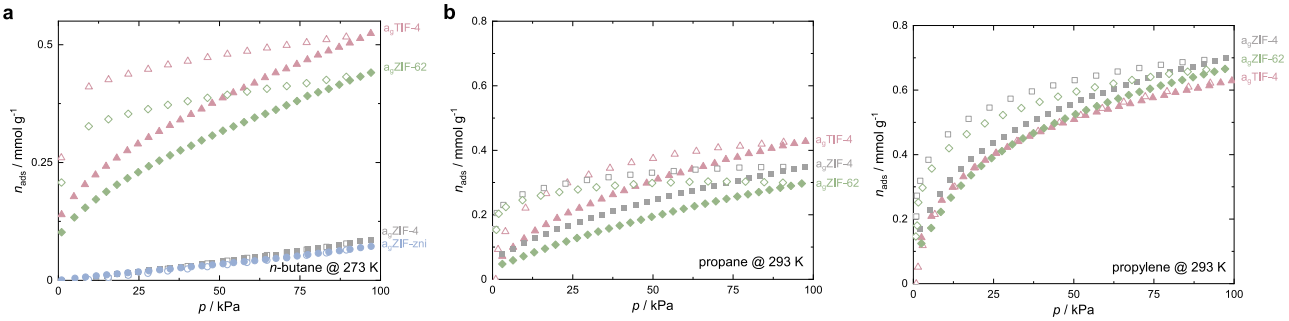

Fig. 4 | Hydrocarbon sorption studies. a *n*-butane sorption isotherms of the ZIF glasses collected at 273 K. **b** Propane and propylene sorption isotherms collected at 293 K. In all panels, adsorption and desorption branches are shown as closed and open symbols, respectively.

minor influence on V_{pore}. Moreover, the finding that V_{pore} of a$_T$ZIF-4, a$_g$ZIF-4 and a$_g$ZIF-zni are similar is in line with our analysis of the FSDP of the scattering function, as well as the previous observation that a$_T$ZIF-4 and a$_g$ZIF-4 are located at the same place on the potential energy landscape of Zn(im)$_2$[21].

For comparison, we collected additional CO_2 sorption isotherms of all materials at 273 K (Supplementary Figs. 49, 50). Here, we see again the highest capacity for ZIF-4 (2.64 mmol g^{-1}) followed by ZIF-62 (1.87 mmol g^{-1}) and TIF-4 (1.43 mmol g^{-1}) whereas the amorphous materials (a$_T$ZIF-4, a$_g$ZIF-4, a$_g$ZIF-zni, a$_g$ZIF-62, a$_g$TIF-4), as well as the materials adopting the zni topology (zniTZIF-4, ZIF-zni), show lower uptakes in the range from 0.81 to 1.21 mmol g^{-1} (Supplementary Table 6). As expected, the drastic differences in V_{pore} of the various ZIF materials are not observable in the CO_2 sorption data collected at 273 K, since data are only collected up to about 0.03p/p_0. Previous works used CO_2 sorption data of ZIF glasses recorded at 273 K to calculate pore size distributions (PSDs) of the materials with the nonlocal density functional theory (NLDFT) method[82] applying a model for carbon materials with slit pores. In our analysis, we found that the PSDs for the crystalline ZIFs derived by this model are in strong disagreement with the theoretical PSDs calculated based on the corresponding crystal structures (Supplementary Methods 9.3). The disagreement is explained by a mismatch of pore geometry and effective adsorption potential of the ZIFs with the carbon-based NLDFT model. Since the NLDFT model cannot reproduce the theoretical PSDs of the crystalline ZIFs, we conclude that this model is inadequate to examine the PSDs of the ZIF glasses as well. We hope that future statistical models for CO_2 gas sorption will be able to safely reproduce the porous features of crystalline ZIFs so that these models could also be used to shed light on the pore size distribution of ZIF glasses[83].

Density determination

The V_{pore} quantified from the CO_2 sorption data recorded at 195 K allows the determination of ρ_{app} of the ZIF glasses. As stated above, ρ_{app} of porous ZIF glasses is unknown so far, since He pycnometry (the established method for density determination of small volume powder samples) only allows determining ρ_{skl} (He penetrates also into the micropores of the materials)[84]. Nevertheless, ρ_{app} is one of the key material properties not only for technological applications but also as a boundary condition for computational modelling of such non-equilibrium amorphous materials[51,85].

Here, ρ_{app} of the ZIF glasses is determined according to the following procedure. At first, we calculated the theoretical void fraction (tVF) for crystalline ZIF-4 and ZIF-zni based on their crystal structures (tVF$_{ZIF\text{-}4}$ = 28.7%, tVF$_{ZIF\text{-}zni}$ = 7.5%; Fig. 1b) and compared these values to the experimental void fraction (eVF = V_{pore}·ρ_{cryst}) calculated from V_{pore} and the crystallographic densities (ρ_{cryst}; see Supplementary Methods 9.4 for further details). For both crystalline ZIFs, we found a good agreement between theory and experiment (eVF$_{ZIF\text{-}4}$ = 30.6%, eVF$_{ZIF\text{-}zni}$ = 6.2%). We note that a similar comparison of the tVFs to the eVFs for crystalline ZIF-62 and TIF-4 is challenging due to the disorder of the secondary bulky linkers in their crystal structures. Subsequently, the V_{pore} of the crystalline ZIF-4, ZIF-zni, ZIF-62 and TIF-4 was plotted against their ρ_{cryst} (Fig. 3d). The data could be very well fitted with an exponential function (R^2 = 0.998, see Supplementary Methods 9.4), which then is used to calculate ρ_{app} of the glasses from their experimental pore volumes (Table 1). In correspondence to their quite similar V_{pore}, we find comparable apparent densities for all glasses in the range from 1.35 to 1.38 cm^3 g^{-1}. Importantly, these densities are up to 20% lower than the skeletal densities (ρ_{skl}) previously determined for ZIF glasses by He pycnometry[23]. Additionally, our data suggest that the density values previously obtained via Archimedes' principle are also too high[62,63], since ethanol was utilized as the soaking solvent which might also penetrate (at least partially) into the glasses' micropores. Based on the pore volumes and densities derived by our method, we further estimate a void fraction between 14% and 16% for the ZIF glasses (see Supplementary Methods 9.2).

Hydrocarbon physisorption studies

Since reliable information on the PSDs of the ZIF glasses could not be obtained from the CO_2 sorption isotherms, we intended to get deeper insights into their pore sizes via hydrocarbon sorption (*n*-butane at 273 K, propane and propylene at 293 K, Fig. 4). In accordance with our previous study on hydrocarbon sorption in a$_g$ZIF-62[30], we found comparable adsorption of *n*-butane for a$_g$ZIF-62 and a$_g$TIF-4. The isotherms are of Type I shape (Langmuir), typical for adsorption in microporous solids, and feature a strong hysteresis, signifying diffusion limitations of *n*-butane in the narrow micropores of the ZIF glasses. Calculation of the void volume occupied by *n*-butane close to saturation ($p \approx 95$ kPa, $p/p_0 \approx 0.95$) and comparison with the void volume determined via CO_2 sorption signifies that *n*-butane is only able to access about 35–42% of the void space available for CO_2 in a$_g$ZIF-62 and a$_g$TIF-4 (Supplementary Table 9).

Surprisingly, a$_g$ZIF-4 and a$_g$ZIF-zni do not adsorb any *n*-butane in their pores but only on the external surface, resulting in isotherms with very little uptake. The contrasting sorption properties of a$_g$ZIF-4 and a$_g$ZIF-zni compared to a$_g$ZIF-62 and a$_g$TIF-4 indicate important differences in the pore structure of these glasses. The larger kinetic diameter of *n*-butane (4.3 Å)[75] compared to CO_2 (3.3 Å)[75] signifies that the pore limiting diameter of a$_g$ZIF-4 and a$_g$ZIF-zni is smaller than the one of the glasses featuring a secondary bulky imidazolate linker (a$_g$ZIF-62 and a$_g$TIF-4). It appears that this difference is not originating from the higher processing temperatures and the slight decomposition of a$_g$ZIF-4 and a$_g$ZIF-zni, since a$_T$ZIF-4 (thermally amorphized at 379 °C, no decomposition) also only adsorb *n*-butane on its external surface and not in the micropores (Supplementary Fig. 53). Thus, the presence of a secondary bulky imidazolate linker appears to be a key parameter for the pore size and pore limiting diameter of the ZIF glasses. Our data indicate that the amorphous frameworks of the composition Zn(im)$_2$

(i.e. a_TZIF-4, a_gZIF-4 and a_gZIF-zni) exhibit narrower pore openings than the framework glasses containing a secondary bulky imidazolate linker (i.e. a_gZIF-62 and a_gTIF-4). Interestingly, small amounts of *n*-butane (0.14 mmol g^{-1}) are adsorbed in a_gZIF-4 at 293 K and 95 kPa, suggesting that the higher kinetic energy of the gas molecules at 293 K allows some penetration in the pores of the glass, even though the *n*-butane uptake of a_gZIF-4 is still significantly lower than the *n*-butane uptake of the mixed-linker ZIF glasses (Supplementary Fig. 56, Supplementary Table 7).

In contrast, propane (kinetic diameter 4.3 Å) and propylene (kinetic diameter 4.5 Å) sorption isotherms at 293 K feature a Langmuir-shape (typical for adsorption in micropores) and show comparable uptakes for all the investigated ZIF glasses (Fig. 4b, c, Supplementary Table 7). In accordance with our recent findings, we see a much higher adsorption affinity for propylene over propane[30] (Supplementary Figs. 57–59). This trend is already present in the crystalline parent materials ZIF-62 and TIF-4 (Supplementary Figs. 58, 59). Except for propylene sorption in a_gTIF-4, significant hystereses again point towards gas diffusion limitations, further confirming the narrow micropores of the ZIF glasses. Additional propane and propylene sorption isotherms recorded at 313 K show that the uptake of both gases at a pressure of 95 kPa is reduced compared to 293 K, while a strongly hysteretic sorption behaviour is still apparent (Supplementary Figs. 60, 61, Supplementary Table 7). Hence, diffusion of these gases in and out of the glass frameworks is still kinetically hindered at 313 K.

Discussion

We investigated the porosity of a compositional series of ZIF glasses in detail, determined their micropore volumes, and compared them to their crystalline framework precursors. This series includes ZIF materials containing only the small im^- linker (ZIF-4 and ZIF-zni) and others, featuring a secondary bulky imidazolate linker (bim^- or $mbim^-$) next to im^- (ZIF-62 and TIF-4). All glasses are found to exhibit CO_2-accessible microporosity and specific pore volumes in the range from 0.10 to 0.12 $cm^3\,g^{-1}$. This also includes a_gZIF-4 and a_gZIF-zni whose open pore space was so far understood as being inaccessible for gases[21,50]. We thus conclude that microporosity is an intrinsic feature of the class of ZIF glasses, which is a huge benefit compared to conventional inorganic glasses, whose microporosity typically must be generated via elaborate post-treatment methods (e.g. leaching procedures)[86].

The specific pore volumes of the ZIF glasses provided a means to calculate the apparent densities of these glasses. The apparent densities are much lower than the previously reported skeletal densities of ZIF glasses and lie in between the density of the most porous glass former ZIF-4 and its most dense (but still microporous) polymorph ZIF-zni. The fact that the density of a_gZIF-62 (ρ_{app} = 1.35 $cm^3\,g^{-1}$) is higher than the density of crystalline ZIF-62 (ρ_{cryst} = 1.29 $cm^3\,g^{-1}$) is in accordance with the negative Clapeyron-slope behaviour reported for ZIF-62 (i.e. melting point lowering with increasing pressure)[87]. Our data suggest a similar behaviour for TIF-4 (ρ_{cryst}(TIF-4) = 1.32 g cm^{-3}, ρ_{app}(a_gTIF-4) = 1.35 g cm^{-3}). In turn, the higher density of ZIF-zni (ρ_{cryst}(ZIF-zni) = 1.54 g cm^{-3}) compared to the corresponding glass (ρ_{app}(a_gZIF-zni) = 1.36 g cm^{-3}) suggest a positive slope of the melting curve and thus conventional melting behaviour (i.e. an increasing melting point with increasing pressure). Moreover, ZIF-4 transforms completely to its denser polymorph with **zni** topology (zni_TZIF-4) before melting occurs and thus is also expected to show a positive Clapeyron slope behaviour.

We generally find slightly lower specific pore volumes and slightly higher densities for a_gZIF-4 and a_gZIF-zni compared to the ZIF glasses containing a secondary bulky imidazolate-type linker. This proves the importance of the bulky linker for a less dense packing of the molecular building units in the glass state[15,38,42], and is also in line with systematic differences of the glasses' ΔQ_{FSDP}, suggesting lower MRO in the glasses containing two different linkers. The important structural differences of the glasses with and without the secondary bulky linkers are further corroborated by hydrocarbon sorption experiments, showing that a_gZIF-62 and a_gTIF-4 adsorb *n*-butane at 273 K, while a_gZIF-4 and a_gZIF-zni do not. Apparently, the presence of the secondary bulky imidazolate-type linkers in a_gZIF-62 and a_gTIF-4 ensures that the glass network is more accessible to larger guests. This is in stark contrast with the porosity features of the corresponding crystalline ZIF phases, where more bulky linkers result in a significant reduction of pore volume and increased steric hindrance for the diffusion of larger molecules.

The present study provides important insights into the porosity of MOF glasses and thus contributes to the understanding of the structure of such glasses. Our findings suggest that conventional porosity design principles, as established for crystalline MOFs and crystalline framework materials in general[1,2,33], cannot be applied for their glassy state. Rather new design concepts for tuning and adjusting the porosity and sorption selectivity of MOF glasses must be developed. We envision that principles which have already been established for other amorphous porous materials may be adaptable for MOF glasses. An example is porous polymers, such as polymers with intrinsic microporosity (PIMs), where molecular building blocks, which facilitate inefficient packing of the polymer chains, result in enhanced porosity[88–91]. Following this route, we propose that via implementation of larger and asymmetric linkers the porosity of MOF glasses is tuneable far beyond the state of the art, opening the door for the development of much more porous MOF glasses with tailored porosity.

Methods

Materials synthesis

The synthesis routes for ZIF-4 (chemical composition $Zn(im)_2$) and ZIF-62 (chemical composition $Zn(im)_{1.65}(bim)_{0.35}$) were reproduced as stated in our previous publication[30]. $Zn(NO_3)_2{\cdot}6H_2O$ (4.0 mmol) and either only imidazole (13.2 mmol; for ZIF-4) or imidazole and benzimidazole (11.55 mmol imidazole, 1.66 mmol benzimidazole; for ZIF-62) were dissolved in 90 mL *N*,*N*-dimethylformamide (DMF). The obtained solution was divided into ten 9 mL portions, which were transferred into ten 12 mL borosilicate vials. The sealed reaction vials were transferred to an oven preheated to 100 °C and kept there for 7 days. After cooling to room temperature, the reaction volumes were recombined, and the formed crystals were filtered off and washed three times with about 20 mL DMF, followed by drying at 200 °C under a dynamic vacuum ($p \sim 10^{-4}$ kPa) overnight. ZIF-zni was synthesized after a modified solvothermal synthesis route based on ZIF-4 by replacing the original solvent DMF with ethanol. TIF-4 (chemical composition: $(Zn(im)_{1.68}(mbim)_{0.32})$ was synthesized after the same procedure as ZIF-62 by replacing the secondary bulky linker benzimidazole by 5-methylbenzimidazole in the synthesis. Based on the four crystalline materials, their thermal products were obtained via thermal treatment in a TGA/DSC apparatus (see Supplementary Methods 5.2).

X-ray powder diffraction (XRPD)

XRPD patterns were recorded at room temperature on a Siemens D5005 diffractometer in Bragg–Brentano geometry. Data were collected with CuK_α radiation in the range from 5° to 50° 2θ with a step size of 0.02°. Finely ground samples (crystalline or glassy) were deposited on a glass holder or a single crystal zero background sample holder made of silicon (cut along the (610) plane). For phase identification, structureless profile fits (Pawley method[64]) were performed with the TOPAS academic v6 software[92].

Fourier transform infra-red (FTIR) spectroscopy

Fourier transform infra-red (FTIR) spectroscopy was carried out on a Perkin Elmer SpectrumTwo FTIR spectrometer ($\tilde{\nu}$ = 400–4000 cm^{-1}) in

reflection mode using a diamond ATR (attenuated total reflectance) unit. Powdered samples were placed on the diamond ATR unit and carefully compressed with a stamp for the measurement.

Scanning electron microscopy (SEM)

Scanning electron microscopy (SEM) imaging was performed with a Hitachi S-4500 instrument. For measurements, samples were placed on a conductive adhesive pad. Imaging was done with 1 kV accelerating voltage on a secondary electron detector. All investigated samples were ground and taken from the sorption tubes after the conduction of physisorption measurements before imaging.

Nuclear magnetic resonance (NMR) spectroscopy

Solution ^{1}H NMR spectroscopy was performed on digested crystalline and glassy ZIF samples with Bruker DPX-300, DPX 500 or Agilent DD2 500 spectrometers. The solid samples were digested before the measurement using DMSO-d_6 (0.5 mL) and DCl/D_2O (35 wt%, one drop, <0.1 mL) as solvents. The data were processed with the MestReNova (v14.2.0) software. Data were referenced to the residual proton signal of DMSO and chemical shifts are given relative to tetramethylsilane.

Thermal analysis

Differential scanning calorimetry measurements (DSC) were performed on a DSC 25 from TA Instruments under a constant nitrogen flow (50 mL min^{-1}). Before the measurement, the samples were ground and placed in a hermitically sealed aluminium crucible and a hole was pinched into the lid of the sealed crucible. Simultaneous thermogravimetric analysis/differential scanning calorimetry (TGA/DSC) measurements were conducted on an STA 504 instrument or SDT 650 from TA Instruments under a constant argon flow (4 L h^{-1}) for STA 504 or a nitrogen flow (100 mL min^{-1}) for SDT 650 on powdered samples. Data were processed and evaluated using the TRIOS (v5.1.0.46403) software from TA instruments. The melting temperatures (T_m) are determined as the peak offset, the glass transition temperatures (T_g) as the peak onset, whereas all other derived temperatures are defined as the peak temperature. The enthalpies are determined from the integral of the corresponding signal.

Isothermal gas physisorption

Low-pressure experiments up to 100 kPa were performed with a Quantachrome iQ MP porosimeter. Sample quantities of about 100 mg (for glasses) and at least 50 mg (for all others) were used for the experiments. Prior to the first measurement, the ground samples were degassed under a dynamic vacuum ($p \approx 10^{-5}$ kPa) at 200 °C for 2 h. Gas sorption isotherms were measured with N_2 (77 K, liquid nitrogen), Ar (87 K, 3P Instruments CryoTune with liquid nitrogen), CO_2 (195 K, dry ice/*iso*-propanol and 273 K, thermostatic bath) and *n*-butane (273 and 293 K, thermostatic bath), propane and propylene (293 and 313 K, thermostatic bath). Between measurements, samples were degassed under a dynamic vacuum ($p \approx 10^{-5}$ kPa) at ambient temperature for ~3 h. After adsorption measurements with *n*-butane, the samples were again heated to 200 °C for 30 min under a dynamic vacuum ($p \approx 10^{-5}$ kPa). High-pressure CO_2 adsorption measurements up to 4130 kPa were conducted using a Microtrac Bel Belsorp VC instrument. The sample holder was filled with about 300 mg of pre-evacuated sample (200 °C in dynamic vacuum for 2 h) and installed in the isothermal box of the instrument, which was kept at 298 K. The sample was evacuated prior to the measurement.

X-ray total scattering

X-ray total scattering data for ZIF-4, a_TZIF-4, zni_TZIF-4, a_gZIF-4, ZIF-zni, a_gZIF-zni and a_gZIF-62 were collected at beamline I15-1 of Diamond Light Source (DLS, UK) using a monochromatic X-ray beam (λ = 0.161669 Å, 76.7 keV). Samples were finely ground before loading into 1.5 mm (outer diameter) borosilicate capillaries. X-ray total scattering data for TIF-4 and a_gTIF-4 were collected at beamline P02.1 at Deutsches Elektronen-Synchrotron (DESY, Germany) using a monochromatic X-ray beam (λ = 0.20734 Å, 60 keV). The samples were placed in a 1 mm (outer diameter) quartz glass capillary. For all datasets, background subtraction was performed with scattering data collected from an empty capillary. Background subtraction, multiple, container and Compton scattering, as well as absorption were done with the GudrunX programme[93]. The normalized reciprocal space data ($S(Q)$, see Supplementary Fig. 41 for corresponding Q_{max} values) were Fourier transformed to yield the X-ray pair distribution functions (XPDFs) in the form of $D(r)$[69,94].

Data availability

The authors declare that all data supporting the findings of this study are available within the article and its supplementary information files. The corresponding raw data are available on request from the corresponding author S.H.

References

1. Yaghi, O. M. et al. Reticular synthesis and the design of new materials. *Nature* **423**, 705–714 (2003).
2. Tranchemontagne, D. J., Mendoza-Cortés, J. L., O'Keeffe, M. & Yaghi, O. M. Secondary building units, nets and bonding in the chemistry of metal-organic frameworks. *Chem. Soc. Rev.* **38**, 1257–1283 (2009).
3. Stock, N. & Biswas, S. Synthesis of metal-organic frameworks (MOFs): routes to various MOF topologies, morphologies, and composites. *Chem. Rev.* **112**, 933–969 (2012).
4. Yuan, S. et al. Stable metal-organic frameworks: design, synthesis, and applications. *Adv. Mater.* **30**, 1704303 (2018).
5. Lin, R. B., Xiang, S., Xing, H., Zhou, W. & Chen, B. Exploration of porous metal-organic frameworks for gas separation and purification. *Coord. Chem. Rev.* **378**, 87–103 (2019).
6. Kreno, L. E. et al. Metal-organic framework materials as chemical sensors. *Chem. Rev.* **112**, 1105–1125 (2012).
7. Lin, Y., Kong, C., Zhang, Q. & Chen, L. Metal-organic frameworks for carbon dioxide capture and methane storage. *Adv. Energy Mater.* **7**, 1601296 (2016).
8. Furukawa, H., Cordova, K. E., O'Keeffe, M. & Yaghi, O. M. The chemistry and applications of metal-organic frameworks. *Science* **341**, 1230444 (2013).
9. Horcajada, P. et al. Metal-organic frameworks in biomedicine. *Chem. Rev.* **112**, 1232–1268 (2012).
10. Baumann, A. E., Burns, D. A., Liu, B. & Thoi, V. S. Metal-organic framework functionalization and design strategies for advanced electrochemical energy storage devices. *Commun. Chem.* **2**, 86 (2019).
11. Stavila, V., Talin, A. A. & Allendorf, M. D. MOF-based electronic and opto-electronic devices. *Chem. Soc. Rev.* **43**, 5994–6010 (2014).
12. Bennett, T. D., Coudert, F. X., James, S. L. & Cooper, A. I. The changing state of porous materials. *Nat. Mater.* **20**, 1179–1187 (2021).
13. Pallach, R. et al. Frustrated flexibility in metal-organic frameworks. *Nat. Commun.* **12**, 4097 (2021).
14. Bennett, T. D. & Cheetham, A. K. Amorphous metal-organic frameworks. *Acc. Chem. Res.* **47**, 1555–1562 (2014).
15. Fonseca, J., Gong, T., Jiao, L. & Jiang, H. L. Metal-organic frameworks (MOFs) beyond crystallinity: amorphous MOFs, MOF liquids and MOF glasses. *J. Mater. Chem. A* **9**, 10562–10611 (2021).
16. Bennett, T. D. & Horike, S. Liquid, glass and amorphous solid states of coordination polymers and metal-organic frameworks. *Nat. Rev. Mater.* **3**, 431–440 (2018).
17. Simonov, A. & Goodwin, A. L. Designing disorder into crystalline materials. *Nat. Rev. Chem.* **4**, 657–673 (2020).

18. Cheetham, A. K., Bennett, T. D., Coudert, F. X. & Goodwin, A. L. Defects and disorder in metal organic frameworks. *Dalton Trans.* **45**, 4113–4126 (2016).
19. Sapnik, A. F. et al. Mixed hierarchical local structure in a disordered metal-organic framework. *Nat. Commun.* **12**, 2062 (2021).
20. Jiang, G. et al. Glassy metal-organic-framework-based quasi-solid-state electrolyte for high-performance lithium-metal batteries. *Adv. Funct. Mater.* **31**, 2104300 (2021).
21. Bennett, T. D. et al. Hybrid glasses from strong and fragile metal-organic framework liquids. *Nat. Commun.* **6**, 8079 (2015).
22. Tao, H., Bennett, T. D. & Yue, Y. Melt-quenched hybrid glasses from metal-organic frameworks. *Adv. Mater.* **29**, 1601705 (2017).
23. Bennett, T. D. et al. Melt-quenched glasses of metal-organic frameworks. *J. Am. Chem. Soc.* **138**, 3484–3492 (2016).
24. Horike, S., Nagarkar, S. S., Ogawa, T. & Kitagawa, S. A new dimension for coordination polymers and metal–organic frameworks: towards functional glasses and liquids. *Angew. Chem. Int. Ed.* **59**, 6652–6664 (2020).
25. Horike, S., Ma, N., Fan, Z., Kosasang, S. & Smedskjaer, M. M. Mechanics, ionics, and optics of metal-organic framework and coordination polymer glasses. *Nano Lett.* **21**, 6382–6390 (2021).
26. Tanaka, K. et al. High Li-ion conductivity in $Li\{N(SO_2F)_2\}(NCCH_2CH_2CN)_2$ molecular crystal. *Nano Lett.* **20**, 8200–8204 (2020).
27. Ogawa, T. et al. Coordination polymer glass from a protic ionic liquid: proton conductivity and mechanical properties as an electrolyte. *Chem. Sci.* **11**, 5175–5181 (2020).
28. Wang, Y. et al. A MOF glass membrane for gas separation. *Angew. Chem. Int. Ed.* **59**, 4365–4369 (2020).
29. Li, J. et al. Coordination polymer glasses with lava and healing ability for high-performance gas sieving. *Angew. Chem. Int. Ed.* **60**, 21304–21309 (2021).
30. Frentzel-Beyme, L., Kloss, M., Kolodzeiski, P., Pallach, R. & Henke, S. Meltable mixed-linker zeolitic imidazolate frameworks and their microporous glasses—from melting point engineering to selective hydrocarbon sorption. *J. Am. Chem. Soc.* **141**, 12362–12371 (2019).
31. Tuffnell, J. M. et al. Novel metal-organic framework materials: Blends, liquids, glasses and crystal-glass composites. *Chem. Commun.* **55**, 8705–8715 (2019).
32. Madsen, R. S. K. et al. Ultrahigh-field ^{67}Zn NMR reveals short-range disorder in zeolitic imidazolate framework glasses. *Science* **367**, 1473–1476 (2020).
33. Freund, R. et al. 25 Years of reticular chemistry. *Angew. Chem. Int. Ed.* **60**, 23946–23974 (2021).
34. Park, K. S. et al. Exceptional chemical and thermal stability of zeolitic imidazolate frameworks. *PNAS* **103**, 10186–10191 (2006).
35. Tian, Y. Q. et al. Design and generation of extended zeolitic metal-organic frameworks (ZMOFs): synthesis and crystal structures of zinc(II) imidazolate polymers with zeolitic topologies. *Chem. Eur. J.* **13**, 4146–4154 (2007).
36. Noh, K., Lee, J. & Kim, J. Compositions and structures of zeolitic imidazolate frameworks. *Isr. J. Chem.* **58**, 1075–1088 (2018).
37. Ríos Gómez, M. L., Lampronti, G. I., Yang, Y., Mauro, J. C. & Bennett, T. D. Relating structural disorder and melting in complex mixed ligand zeolitic imidazolate framework glasses. *Dalton Trans.* **49**, 850–857 (2020).
38. Hou, J. et al. Halogenated metal-organic framework glasses and liquids. *J. Am. Chem. Soc.* **142**, 3880–3890 (2020).
39. Zhou, C. et al. Polymorph formation for a zeolitic imidazolate framework composition - $Zn(Im)_2$. *Microporous Mesoporous Mater.* **265**, 57–62 (2018).
40. Longley, L. et al. Flux melting of metal-organic frameworks. *Chem. Sci.* **10**, 3592–3601 (2019).
41. Bumstead, A. M. et al. Investigating the melting behaviour of polymorphic zeolitic imidazolate frameworks. *CrystEngComm* **22**, 3627–3637 (2020).
42. Zhou, C. et al. Metal-organic framework glasses with permanent accessible porosity. *Nat. Commun.* **9**, 5042 (2018).
43. Böhme, U. et al. Ethene/ethane and propene/propane separation via the olefin and paraffin selective metal-organic framework adsorbents CPO-27 and ZIF-8. *Langmuir* **29**, 8592–8600 (2013).
44. Yang, J. et al. Principles of designing extra-large pore openings and cages in zeolitic imidazolate frameworks. *J. Am. Chem. Soc.* **139**, 6448–6455 (2017).
45. Banerjee, R. et al. High-throughput synthesis of zeolitic imidazolate frameworks and application to CO_2 capture. *Science* **319**, 939–943 (2008).
46. Li, K. et al. Zeolitic imidazolate frameworks for kinetic separation of propane and propene. *J. Am. Chem. Soc.* **131**, 10368–10369 (2009).
47. Hartmann, M., Böhme, U., Hovestadt, M. & Paula, C. Adsorptive separation of olefin/paraffin mixtures with ZIF-4. *Langmuir* **31**, 12382–12389 (2015).
48. Louis, F. B. et al. Porous purple glass – a cobalt imidazolate glass with accessible porosity from a meltable cobalt imidazolate framework. *J. Mater. Chem. A* **7**, 985–990 (2019).
49. Bennett, T. D. et al. Structure and properties of an amorphous metal-organic framework. *Phys. Rev. Lett.* **104**, 115503 (2010).
50. Thornton, A. W. et al. Porosity in metal-organic framework glasses. *Chem. Commun.* **52**, 3750–3753 (2016).
51. Gaillac, R. et al. Liquid metal-organic frameworks. *Nat. Mater.* **16**, 1149–1154 (2017).
52. Gaillac, R., Pullumbi, P., Bennett, T. D. & Coudert, F. X. Structure of metal-organic framework glasses by ab initio molecular dynamics. *Chem. Mater.* **32**, 8004–8011 (2020).
53. Qiao, A. et al. A metal-organic framework with ultrahigh glass-forming ability. *Sci. Adv.* **4**, eaao6827 (2018).
54. Gidley, D. W., Peng, H. G. & Vallery, R. S. Positron annihilation as a method to characterize porous materials. *Annu. Rev. Mater. Res.* **36**, 49–79 (2006).
55. Sing, K. S. W. Reporting physisorption data for gas/solid systems with special reference to the determination of surface area and porosity (Recommendations 1984). *Pure & Appl. Chem.* **57**, 603–619 (1985).
56. Thommes, M. et al. Physisorption of gases, with special reference to the evaluation of surface area and pore size distribution (IUPAC Technical Report). *Pure Appl. Chem.* **87**, 1051–1069 (2015).
57. Cychosz, K. A. & Thommes, M. Progress in the Physisorption Characterization of Nanoporous Gas Storage Materials. *Engineering* **4**, 559–566 (2018).
58. Islamoglu, T. et al. Are you using the right probe molecules for assessing the textural properties of metal-organic frameworks? *J. Mater. Chem. A* **10**, 157–173 (2022).
59. Vishnyakov, A., Ravikovitch, P. I. & Neimark, A. V. Molecular level models for CO2 sorption in nanopores. *Langmuir* **15**, 8736–8742 (1999).
60. Samios, S., Stubos, A. K., Papadopoulos, G. K., Kanellopoulos, N. K. & Rigas, F. The structure of adsorbed CO2 in slitlike micropores at low and high temperature and the resulting micropore size distribution based on GCMC simulations. *J. Colloid Interface Sci.* **224**, 272–290 (2000).
61. Decker, G. E. & Bloch, E. D. Using helium pycnometry to study the apparent densities of metal-organic frameworks. *ACS Appl. Mater. Interfaces* **13**, 51925–51932 (2021).
62. Stepniewska, M., Østergaard, M. B., Zhou, C. & Yue, Y. Towards large-size bulk ZIF-62 glasses via optimizing the melting conditions. *J. Non-Cryst. Solids* **530**, 119806 (2020).

63. Qiao, A. et al. Deformation mechanism of a metal-organic framework glass under indentation. *Phys. Chem. Chem. Phys.* **23**, 16923–16931 (2021).
64. Pawley, G. S. Unit-cell refinement from powder diffraction scans. *J. Appl. Cryst.* **14**, 357–361 (1981).
65. Phan, A. et al. Synthesis, structure, and carbon dioxide capture properties of zeolitic imidazolate frameworks. *Acc. Chem. Res.* **43**, 58–67 (2010).
66. Wu, T., Bu, X., Zhang, J. & Feng, P. New zeolitic imidazolate frameworks: from unprecedented assembly of cubic clusters to ordered cooperative organization of complementary ligands. *Chem. Mater.* **20**, 7377–7382 (2008).
67. Lehnert, R. & Seel, F. Darstellung und Kristallstruktur des Mangan(II)- und Zink(II)-Derivates des Imidazols. *Z. anorg. allg. Chem.* **464**, 187–194 (1980).
68. Bennett, T. D. et al. Thermal amorphization of zeolitic imidazolate frameworks. *Angew. Chem. Int. Ed.* **50**, 3067–3071 (2011).
69. Keen, D. A. A comparison of various commonly used correlation functions for describing total scattering. *J. Appl. Cryst.* **34**, 172–177 (2001).
70. Elliott, S. R. Medium-range structural order in covalent amorphous solids. *Nature* **354**, 445–452 (1991).
71. Elliott, S. R. Origin of the first sharp diffraction peak in the structure factor of covalent glasses. *Phys. Rev. Lett.* **67**, 711–714 (1991).
72. Salmon, P. S. Real space manifestation of the first sharp diffraction peak in the structure factor of liquid and glassy materials. *Proc. R. Soc. Lond. A* **445**, 351–365 (1994).
73. Ramesh Rao, N. et al. Structural correlations in GexSe1−x glasses—a neutron diffraction study. *J. Non-Cryst. Solids* **240**, 221–231 (1998).
74. Lucovsky, G. & Phillips, J. C. Symmetry determined medium range order (MRO) contributions to the first sharp diffraction peak (FSDP) in non-crystalline oxide and chalcogenide glasses. *Phys. Status Solidi* **246**, 1806–1812 (2009).
75. Breck, D. W. *Zeolite Molecular Sieves: Structure, Chemistry, and Use* (Wiley, 1973).
76. Marsh, H. & Brand, B. The characterization of microporous carbons by means of the Dubinin–Radushkevich equation. *J. Colloid Interface Sci.* **33**, 101–116 (1970).
77. Klank, D., Blum, C. & Schneider, D. Adsorptionsstudien mit CO2—Flüssigkeit oder Trockeneis? *Chem. Ing. Tech.* **92**, 1871–1872 (2020).
78. Dantas, S., Struckhoff, K. C., Thommes, M. & Neimark, A. V. Phase behavior and capillary condensation hysteresis of carbon dioxide in mesopores. *Langmuir* **35**, 11291–11298 (2019).
79. Branton, P. J., Hall, P. G., Treguer, M. & Sing, K. S. W. Adsorption of carbon dioxide, sulfur dioxide and water vapour by MCM-41, a model mesoporous adsorbent. *J. Chem. Soc. Faraday Trans.* **91**, 2041–2043 (1995).
80. Brunauer, S., Emmett, P. H. & Teller, E. Adsorption of gases in multimolecular layers. *J. Am. Chem. Soc.* **60**, 309–319 (1938).
81. Schröder, C. A., Baburin, I. A., van Wüllen, L., Wiebcke, M. & Leoni, S. Subtle polymorphism of zinc imidazolate frameworks: temperature-dependent ground states in the energy landscape revealed by experiment and theory. *CrystEngComm* **15**, 4036–4040 (2013).
82. Lastoskie, C., Gubbins, K. E. & Quirke, N. Pore size distribution analysis of microporous carbons: a density functional theory approach. *J. Phys. Chem.* **97**, 4786–4796 (1993).
83. Kikkinides, E. S., Monson, P. A. & Valiullin, R. Sorption isotherm reconstruction and extraction of pore size distributions for serially connected pore model (SCPM) structures employing algorithmic and statistical models. *J. Phys. Chem. C* **124**, 21591–21607 (2020).
84. Nguyen, H. G. T., Horn, J. C., Bleakney, M., Siderius, D. W. & Espinal, L. Understanding material characteristics through signature traits from helium pycnometry. *Langmuir* **35**, 2115–2122 (2019).
85. To, T. et al. Fracture toughness of a metal-organic framework glass. *Nat. Commun.* **11**, 2593 (2020).
86. Enke, D., Janowski, F. & Schwieger, W. Porous glasses in the 21st century-a short review. *Microporous Mesoporous Mater.* **60**, 19–30 (2003).
87. Widmer, R. N. et al. Pressure promoted low-temperature melting of metal-organic frameworks. *Nat. Mater.* **18**, 370–376 (2019).
88. Mc Keown, N. B. & Budd, P. M. Polymers of intrinsic microporosity (PIMs): organic materials for membrane separations, heterogeneous catalysis and hydrogen storage. *Chem. Soc. Rev.* **35**, 675–683 (2006).
89. Das, S., Heasman, P., Ben, T. & Qiu, S. Porous organic materials: strategic design and structure–function correlation. *Chem. Rev.* **117**, 1515–1563 (2017).
90. Park, H. B. et al. Polymers with cavities tuned for fast selective transport of small molecules and ions. *Science* **318**, 254–258 (2007).
91. Butler, B. J. et al. An efficient polymer molecular sieve for membrane gas separations. *Science* **339**, 303–307 (2013).
92. Coelho, A. A. TOPAS and TOPAS-Academic: an optimization program integrating computer algebra and crystallographic objects written in C++. *J. Appl. Cryst.* **51**, 210–218 (2018).
93. Soper, A. K. *GudrunN and GudrunX: Programs for Correcting Raw Neutron and X-ray Diffraction Data to Differential Scattering Cross Section*. Rutherford Appleton Laboratory Technical Report (Rutherford Appleton Laboratory, 2011).
94. Soper, A. K. & Barney, E. R. Extracting the pair distribution function from white-beam X-ray total scattering data. *J. Appl. Cryst.* **44**, 714–726 (2011).

Acknowledgements

This project received funding from TU Dortmund, Deutsche Forschungsgemeinschaft within the Priority Programme SPP1928 COORNETs (Gateway Fellowship to L.F.B. and Start-Up Grant to S.H.) and project 447344931 (S.H.) and was supported by an Exploration Grant of Boehringer Ingelheim Foundation (S.H.). The Fonds der Chemischen Industrie is gratefully acknowledged for awarding a Kekulé-Fellowship to P.K. and a Liebig Fellowship to A.S. The research leading to this result has been supported by the project CALIPSOplus under the Grant Agreement 730872 from the EU Framework Programme for Research and Innovation HORIZON 2020. We thank Diamond Light Source (DLS) for access to beamline I15-1 (CY21604-2) which contributed to the results presented here. Beamline scientists Thomas Forrest and Philip Chater are acknowledged for their support with the X-ray total scattering experiments at DLS. We thank Jianbo Song and Roman Pallach for their help with collecting the data at DLS. We acknowledge DESY (Hamburg, Germany), a member of the Helmholtz Association HGF, for the provision of experimental facilities. Parts of this research were carried out at PETRA III on beamline P02.1 and we thank Alba San Jose Mendez and Volodymyr Baran for assistance in collecting X-ray total scattering data. Beamtime was allocated for proposal I-20210316. Athanasios Koutsianos and Roman Pallach are acknowledged for helping with the experiments at DESY. Volker Brandt is acknowledged for collecting SEM images. We thank Martin Wickenheisser from 3P Instruments for helpful discussions. We acknowledge financial support by Deutsche Forschungsgemeinschaft and Technische Universität Dortmund/TU Dortmund University within the funding program Open Access Costs.

Author contributions

L.F.-B., P.K. and J.-B.W. synthesized the materials and performed and analysed XRPD, FTIR spectroscopy, NMR spectroscopy and thermal analysis experiments. L.F.-B. and P.K. collected and analysed X-ray total

scattering data. L.F.-B. collected and analysed lower-pressure gas physisorption data. A.S. performed high-pressure CO_2 sorption experiments. All authors contributed to discussing the data. L.F.-B. and S.H. wrote the manuscript.

Funding

Open Access funding enabled and organized by Projekt DEAL.

Competing interests

The authors declare no competing interests.

Additional information

Supplementary information The online version contains supplementary material available at https://doi.org/10.1038/s41467-022-35372-5.

Correspondence and requests for materials should be addressed to Sebastian Henke.

Peer review information *Nature Communications* thanks the anonymous reviewer(s) for their contribution to the peer review of this work.